

CrossMark
click for updatesCite this: *J. Mater. Chem. C*, 2016,
4, 5424

Magnetic double-tartaric bridging mono-lanthanide substituted phosphotungstates with photochromic and switchable luminescence properties†

Pengtao Ma, Feng Hu, Rong Wan, Yu Huo, Dongdi Zhang, Jingyang Niu* and
Jingping Wang*

A series of inorganic–organic hybrid double-tartaric bridging mono-lanthanide substituted phosphotungstates with a general formula of $[\text{N}(\text{CH}_3)_4]_6\text{K}_3\text{H}_7[\text{Ln}(\text{C}_4\text{H}_2\text{O}_6)(\alpha\text{-PW}_{11}\text{O}_{39})]_2 \cdot 27\text{H}_2\text{O}$ (Ln = Dy for **1Dy**, Er for **2Er**, and Yb for **3Yb**) have been synthesized by the reactions of $\text{K}_{14}[\text{P}_2\text{W}_{19}\text{O}_{69}(\text{H}_2\text{O})] \cdot 24\text{H}_2\text{O}$ and $\text{LnCl}_3 \cdot 6\text{H}_2\text{O}$ in the presence of tartaric acid and tetramethyl ammonium counterions in an aqueous medium. Crystal structure analyses reveal that **1Dy–3Yb** are isomorphous and are all built from two mono-lanthanide substituted Keggin polyoxoanion fragments joined together by two tartaric ligands. **1Dy–3Yb** exhibit reversible photochromism and they can change from white (for **1Dy** and **3Yb**) or pink (for **2Er**) to blue upon UV irradiation and then their colors gradually recover in the dark for about five days. The solid-state photoluminescence spectra of **1Dy–3Yb** display their characteristic emissions of lanthanide components based on their 4f–4f transitions. Moreover, the fluorescence of **1Dy** displays an effectively switchable behaviour when exposed to UV light, the intensity of the emission band at 573 nm gradually weakens as the irradiation time increases and the intensity drops to 2.4% of the original intensity after 30 minutes. It is noteworthy that the frequency dependence of the ac-susceptibility was found for **1Dy**, suggesting a typical single-molecule magnet (SMM) behavior with an energy barrier of 20 K.

Received 7th March 2016,
Accepted 5th May 2016

DOI: 10.1039/c6tc00960c

www.rsc.org/MaterialsC

Introduction

Multifunctional crystalline materials, as important media for energy conversions between optics, electricity, magnetism, heat and other forms, have attracted considerable interest because of vast potential applications in optical switches, photometry, photomechanics, optoelectronic devices, information storage, magnetic refrigeration, *etc.*¹ In these areas, the fabrication of these materials is performed usually by using a combination of functional organic moieties and metal oxide clusters *via* self-assembly, grafting, doping or intercalation, which can endow such hybrids with new structural features and multiple functionalities as a result of blending of different components.² It is crucial to select appropriate functional building units based on their synergistic effect to effectively construct multifunctional crystalline solid materials with well-established structures.

Henan Key Laboratory of Polyoxometalate Chemistry,
Institute of Molecular and Crystal Engineering, College of Chemistry and Chemical
Engineering, Henan University, Kaifeng, Henan 475004, P. R. China.

E-mail: jyniu@henu.edu.cn, jpwang@henu.edu.cn; Fax: +86-371-23886876

† Electronic supplementary information (ESI) available: X-ray crystallographic details (CIF) and Tables S1 and S2, and Fig. S1–S15. CCDC 1454673 (**1Dy**), 1454674 (**2Er**) and 1454675 (**3Yb**). For ESI and crystallographic data in CIF or other electronic format see DOI: 10.1039/c6tc00960c

Polyoxometalates (POMs) exhibit enormous structural diversities and attractive properties of thermal and oxidative stability, remarkable electronic and magnetic properties, Brønsted acidity, *etc.*, which endow them with great potential to cope with and solve contemporary emerging issues regarding the environment, materials, energy, health and information technologies, *etc.*³ Therefore, POMs can be very good and versatile candidates for the design of various multifunctional materials. An effective strategy to synthesize POM-based multifunctional materials is the incorporation of functional organic moieties and desired metal centers (transition metal or lanthanide (Ln) ions) into POM clusters *via* the self-assembly strategy. Thereby, numerous inorganic–organic hybrid POMs have been obtained, which reveal multi-functional characteristics such as photochromic, thermosensitive, electrochromic and photocatalytic activities.⁴ In particular, photochromic POM hybrid materials have attracted increasing attention. For example, Mialane *et al.* reported two dual photochromic/electrochromic compounds based on cationic spiro-pyrans and Keggin-type POM anions $[\text{PM}_{12}\text{O}_{40}]^{3-}$ (M = W or Mo).⁵ Wang *et al.* selected chiral ammonium cations bis[(*R*)- and (*S*)-1-phenylethyl]amine hydrochloride ((*R,R*)- and (*S,S*)-BPEA) to replace the counterions of $\text{H}_4[\text{PMo}_{11}\text{VO}_{40}] \cdot 32.5\text{H}_2\text{O}$ (PMo_{11}V) and obtained photoswitchable chiral POM complexes (*R,R*)-BPEA- PMo_{11}V and (*S,S*)-BPEA- PMo_{11}V .⁶ Our group reported a

series of multicarboxylic acid functionalized heteropolyoxomolybdates containing $[\text{TeMo}_6\text{O}_{21}]^{2-}$ units, which exhibit intriguing dual thermochromic and photochromic properties.⁷ Shen *et al.* prepared a durable and fast-responsive photochromic and switchable luminescent polyviologen–POM hybrid $[(\text{AV}^{2+})(\text{p-AV})(\text{EuW}_{10}\text{O}_{36})]_n \cdot 2n\text{H}_2\text{O}$.⁸ Nevertheless, to date, there have been few reports on POM-based multifunctional materials exhibiting reversible photochromic, luminescence and magnetic properties.

Considering the multifunctionalities of the luminescence and magnetic properties of POM-based materials, much attention has been paid to Ln-substituted POMs (LSPs) in recent years, in which Ln ions bear rich luminous advantages and interesting magnetic properties as a result of their unique 4f electron configurations.⁹ When it comes to well-known LSPs, there is no doubt that Ln-substituted arsenotungstates (LSAs) have been extensively reported in the past several decades (the collection of LSAs is given in Table S1 in the ESI†). In contrast, Ln-substituted lacunary Keggin-type phosphotungstates (LSLKPs) are very limited. In the past several decades, the main types of LSLKPs have been 2 : 1 and 2 : 2 derivatives. In 1971, Peacock and Weakley firstly reported a chiral C_2 -symmetric anion $[\text{Ln}(\text{PW}_{11}\text{O}_{39})_2]^{n-}$ (Ln = Ce^{III/IV}, Pr^{III}, Eu^{III}, Er^{III}) (Fig. S1a, ESI†).¹⁰ In recent years, our group reported several types of LSLKPs including 2 : 2 types of dimeric $\{[(\alpha\text{-PW}_{11}\text{O}_{39})\text{Ln}(\text{H}_2\text{O})_3]_2\}^{6-}$ (Ln = Nd^{III}, Gd^{III}) (Fig. S1b, ESI†),¹¹ 1D zigzag chain $[(\alpha\text{-PW}_{11}\text{O}_{39})\text{Ln}(\text{H}_2\text{O})_2]^{4-}$ (Ln = Ce^{III}, Eu^{III}) (Fig. S1c, ESI†),^{10b,12} and 1-D linear chain $[\text{Tb}(\text{H}_2\text{O})_2(\alpha\text{-PW}_{11}\text{O}_{39})]^{4-}$ (Fig. S1d, ESI†).¹³ Fang *et al.* synthesized a series of sandwich-type LSLKPs $[(\text{A-XW}_9\text{O}_{34})_2(\text{H}_2\text{OM})_3\text{CO}_3]^{11-}$ (X = P^V, As^V; M = Y^{III}, Eu^{III}, Gd^{III}, Tb^{III}, Dy^{III}, Er^{III}) (Fig. S1e, ESI†).¹⁴ Apart from these typical structural types, some uncommon LSLKPs were also found. Nogueira *et al.* reported a novel 3 : 2-type LSLKP $[\text{Ce}_2(\text{PW}_{10}\text{O}_{28})(\text{PW}_{11}\text{O}_{39})_2]^{17-}$ (Fig. S1f, ESI†) in 2004.¹⁵ In the same year, Francesconi *et al.* reported a tetrameric LSLKP $\{[(\text{Eu}_2\text{PW}_{10}\text{O}_{38})_4(\text{W}_3\text{O}_8(\text{H}_2\text{O})_2(\text{OH})_4)]^{22-}$ (Fig. S1g, ESI†) containing four di-Ln substituted Keggin $[\text{LnPW}_{10}\text{O}_{38}]^{8-}$ units joined together by a $[\text{W}_3\text{O}_8]^{6-}$ fragment.^{10b} Apparently, most of the above-mentioned LSLKPs are purely inorganic, but only a few organic–inorganic LSLKP clusters are found.¹¹ Therefore, we have explored LSLKPs functionalized by organic carboxylic acid ligands since 2009 and this system has been widely exploited. The 2 : 2-type acetate-bridging LSLKPs $\{[(\alpha\text{-PW}_{11}\text{O}_{39})\text{Ln}(\text{H}_2\text{O})(\eta^2, \mu-1, 1)\text{-CH}_3\text{COO}]_2\}^{10-}$ (Fig. S1h, ESI†) were firstly isolated.¹¹ Afterwards, the utilization of dicarboxylic oxalate led to the isolation of 2 : 2-type oxalate-bridging dimeric LSLKPs $\{[(\alpha\text{-PW}_{11}\text{O}_{39})\text{RE}(\text{H}_2\text{O})]_2(\text{C}_2\text{O}_4)\}^{10-}$ (RE = Y^{III}, Dy^{III}, Ho^{III}, Er^{III}) (Fig. S1i, ESI†) and 1D chain-like LSLKP $\{(\alpha\text{-x-PW}_{10}\text{O}_{38})\text{Im}_2(\text{C}_2\text{O}_4)(\text{H}_2\text{O})_2\}^{3-}$ (Fig. S1j, ESI†).¹⁶ To date, carboxylic acids (such as acetic acid or oxalic acid) used in LSLKPs contain no more than two carbon atoms; the introduction of carboxylic acid ligands with more than three carbon atoms to the reaction system may increase the steric hindrance in the structure of the resulting LSLKPs, which brings a great difficulty to the design and synthesis of novel organic–inorganic LSLKPs. Therefore, it is interesting and challengeable to prepare functional LSLKP hybrids using multidentate carboxylic acid ligands with more than two carbon atoms. Recently, we explored

the organic–inorganic LSLKP system in the conventional aqueous solution based on the following considerations: firstly, tartaric acid was selected as a flexible multidentate carboxylic acid ligand, which is apt to coordinate to Ln cations as well as inorganic POM units so as to achieve its organic functionalization. Secondly, the careful selection of organic cations such as imidazolium, quinoline and alkylamine cations can lead to intramolecular proton transfer through the H-bonds between POMs and organic cations, which is desirable for improving the photochemical and photophysical properties of hybrid POM materials. Thirdly, considering the characteristic luminescence and magnetic properties of Ln cations, and especially recently frequently reported single-molecular magnet (SMM) behaviors, we were interested in the investigation of these LSLKP materials with coupled luminescence and SMM behaviors.

In this context, we selected the metastable precursor $[\text{P}_2\text{W}_{19}\text{O}_{69}(\text{H}_2\text{O})]^{14-}$ to react with Ln ions and tartaric acid in the presence of tetramethyl ammonium chloride to prepare functional LSLKP hybrids. Thus, three new organic–inorganic hybrid LSLKPs $[(\alpha\text{-PW}_{11}\text{O}_{39})\text{Ln}(\text{C}_4\text{H}_2\text{O}_6)]^{8-}$ (Ln = Dy(III) for **1Dy**, Er(III) for **2Er**, Yb(III) for **3Yb**) were obtained and structurally characterized, which exhibit a reversible photochromic behavior and the characteristic emissions of Ln components based on 4f–4f transitions. More importantly, **1Dy** exhibits unexpected switchable luminescence and SMM behaviors. This work opens up the avenue for profoundly exploring and preparing POM-based multifunctional crystalline materials and further exploits their increasing multifunctionality in energy conversions between optics, electricity, magnetism, heat and other forms.

Experimental

Materials and methods

All chemicals and solvents were used as purchased without further purification. $\text{K}_{14}[\text{P}_2\text{W}_{19}\text{O}_{69}(\text{H}_2\text{O})] \cdot 24\text{H}_2\text{O}$ was prepared according to the published procedure.¹⁷

Synthesis of $[\text{N}(\text{CH}_3)_4]_6\text{K}_3\text{H}_7[\text{Dy}(\text{C}_4\text{H}_2\text{O}_6)(\alpha\text{-PW}_{11}\text{O}_{39})_2] \cdot 27\text{H}_2\text{O}$ (1Dy**).** $\text{DyCl}_3 \cdot 6\text{H}_2\text{O}$ (0.221 g, 0.600 mmol) was dissolved in 40 mL of deionized water and tartaric acid (0.120 g, 0.800 mmol) was added, resulting in a clear solution. Solid $\text{K}_{14}[\text{P}_2\text{W}_{19}\text{O}_{69}(\text{H}_2\text{O})] \cdot 24\text{H}_2\text{O}$ (2.120 g, 0.465 mmol) was quickly added with vigorous stirring. The solution pH was adjusted to 3.4 by the addition of NaOH solution (2 mol L⁻¹). The solution was heated to 60 °C for 1 h and then tetramethyl ammonium chloride (TMACl) (0.110 g, 1.000 mmol) was added and stirred for 30 min. The resulting solution was filtered and left to evaporate at ambient temperature. Colorless block crystals suitable for X-ray diffraction were collected after several days. Yield: 41.5% (0.858 g). Anal. calcd (%) for **1Dy**: C, 5.49; H, 1.68; N, 1.20. Found: C, 5.63; H, 1.77; N, 1.19. Selected IR (KBr, cm⁻¹): 3445 (br), 3037 (w), 1621 (s), 1484 (s), 1094 (s), 1048 (s), 950 (s), 886 (s), 820 (s), 701 (w).

Synthesis of $[\text{N}(\text{CH}_3)_4]_6\text{K}_3\text{H}_7[\text{Er}(\text{C}_4\text{H}_2\text{O}_6)(\alpha\text{-PW}_{11}\text{O}_{39})_2] \cdot 27\text{H}_2\text{O}$ (2Er**).** The synthesis of **2Er** was similar to **1Dy** except for $\text{ErCl}_3 \cdot 6\text{H}_2\text{O}$ (0.220 g, 0.600 mmol) replacing $\text{DyCl}_3 \cdot 6\text{H}_2\text{O}$. Yield: 37.0% (0.766 g). Anal. calcd (%) for **2Er**: C, 5.48; H, 1.68; N, 1.20. Found: C, 5.79; H, 1.86; N, 1.29. Selected IR (KBr, cm⁻¹): 3457 (br),

3033 (w), 1623 (s), 1484 (s), 1093 (s), 1049 (s), 951 (s), 887 (s), 815 (s), 700 (w).

Synthesis of $[N(CH_3)_4]_6K_3H_7[Yb(C_4H_2O_6)(\alpha-PW_{11}O_{39})]_2 \cdot 27H_2O$ (3Yb). The synthesis of **3Yb** was similar to **1Dy** except for $YbCl_3 \cdot 6H_2O$ (0.220 g, 0.600 mmol) replacing $DyCl_3 \cdot 6H_2O$. Yield: 35.5% (0.736 g). Anal. calcd (%) for **3Yb**: C, 5.47; H, 1.68; N, 1.20. Found: C, 5.90; H, 1.91; N, 1.25. Selected IR (KBr, cm^{-1}): 3458 (br), 3035 (w), 1628 (s), 1484 (s), 1096 (s), 1050 (s), 952 (s), 888 (s), 818 (s), 702 (w).

Physical measurements

IR spectra were recorded on a Bruker VERTEX 70 IR spectrometer using KBr pellets in the range 4000–400 cm^{-1} . C, H and N elemental analyses were performed on an Elementar Vario EL cube CHNS analyzer. Powder X-ray diffraction (PXRD) data were recorded on a Bruker D8 Advance instrument with Cu K α radiation ($\lambda = 1.5418 \text{ \AA}$) in the angular range $2\theta = 5\text{--}50^\circ$ at 293 K. Diffuse reflectance spectra were collected at room temperature on a finely ground sample using a HITACHI U-4100 UV-vis-NIR spectrometer equipped with a 60 mm diameter integrating sphere. The electron paramagnetic resonance (EPR) experiment was performed on a Bruker ER-2000-DSRC10 spectrometer in the X-band at 110 K. Thermogravimetric analyses (TGA) were performed on a NETZSCH STA 449 F5 Jupiter thermal analyzer in flowing N_2 at a heating rate of 10 $^\circ C \text{ min}^{-1}$. Photoluminescence properties were investigated on an EDINBURGH FLS 980 fluorescence spectrophotometer. Magnetic measurements were performed on a Quantum Design SQUID magnetometer (MPMS3 and PPMS-9). Energy-dispersive X-ray spectroscopy (EDS) measurements were performed using a JSM-7610F scanning electron microscope with an OXFORD x-act EDS system.

X-ray crystallography

A good single crystal of **1Dy**, **2Er** or **3Yb** was sealed in a capillary tube for indexing and intensity data collection at 296 K on a Bruker APEX2 CCD diffractometer using graphite-monochromated

Mo K α radiation ($\lambda = 0.71073 \text{ \AA}$). Routine Lorentz and polarization corrections were applied and a multi-scan absorption correction was performed using the SADABS program.¹⁸ These structures were solved by direct methods and refined by full-matrix least-squares on all F^2 data using the SHELXTL program suite.¹⁹ In the final refinement cycles, the W, P, and Ln atoms were refined anisotropically; the O, C and N atoms were refined isotropically. The lattice water molecules were determined by the TGA results. Three disordered K^+ ions were determined by the EDX measurement results. The hydrogen atoms of the organic groups were placed in calculated positions and then refined using a riding model with a uniform value of $U_{iso} = 1.2$ or $1.5U_{eq}$. All H atoms on water molecules were directly included in the molecular formula. The crystal data and structure refinement parameters are listed in Table 1.

Results and discussion

Crystal structures

Single-crystal structural analyses reveal that **1Dy–3Yb** are all isostructural and crystallize in the same orthorhombic space group $Pna2_1$ (Table 1). Therefore, only the structure of **1Dy** is described in detail. Their common structural feature is best described as a dimeric dumbbell-like LSLKP anion $[(\alpha-PW_{11}O_{39})Ln(C_4H_2O_6)]_2^{16-}$ (Ln = Dy(III) for **1Dy**, Er(III) for **2Er**, Yb(III) for **3Yb**). This kind of structural construction is mainly governed by two tartaric acid groups. The structural unit of **1Dy** contains a dimeric LSLKP anion $[(\alpha-PW_{11}O_{39})Dy(C_4H_2O_6)]_2^{16-}$, six $[N(CH_3)_4]^+$ counter cations, twenty seven lattice water molecules, three K^+ ions and seven protons for the charge balance. The dimeric LSLKP anion $[(\alpha-PW_{11}O_{39})Dy(C_4H_2O_6)]_2^{16-}$ consists of two mono-Dy-substituted Keggin units bridged by two organic tartaric acid ligands, which obviously elongate the size of dimeric Keggin-type POMs. Except for the two kinds of acetic acid and oxalate ligands-bridging LSLKPs $\{[(\alpha-PW_{11}O_{39})Ln(H_2O)(\eta^2, \mu-1, 1)CH_3COO]_2\}^{10-}$

Table 1 Crystallographic data for **1Dy–3Yb**

	1Dy	2Er	3Yb
Formula	$C_{32}H_{117}K_3N_6O_{117}P_2W_{22}Dy_2$	$C_{32}H_{117}K_3N_6O_{117}P_2W_{22}Er_2$	$C_{32}H_{117}K_3N_6O_{117}P_2W_{22}Yb_2$
Mr (g mol $^{-1}$)	7006.96	7016.48	7028.04
Cryst. syst.	Orthorhombic	Orthorhombic	Orthorhombic
Space group	$Pna2_1$	$Pna2_1$	$Pna2_1$
$a/\text{\AA}$	22.277(5)	22.1047(14)	22.1006(13)
$b/\text{\AA}$	13.120(3)	13.0665(9)	13.0302(7)
$c/\text{\AA}$	52.440(12)	52.158(4)	51.964(3)
$V (\text{\AA}^3)$	15327(6)	15064.9(18)	14964.3(15)
Z	4	4	4
$D_{calcd} (\text{g cm}^{-3})$	2.854	2.908	2.933
$\mu (\text{mm}^{-1})$	17.501	17.928	18.177
Cryst. size (mm 3)	$0.46 \times 0.4 \times 0.11$	$0.43 \times 0.25 \times 0.22$	$0.50 \times 0.4 \times 0.16$
Limiting indices	$-23 \leq h \leq 26$ $-15 \leq k \leq 15$ $-62 \leq l \leq 48$	$-26 \leq h \leq 19$ $-15 \leq k \leq 15$ $-62 \leq l \leq 61$	$-26 \leq h \leq 25$ $-15 \leq k \leq 1$ $-61 \leq l \leq 55$
No. of reflns collected	69992	68411	72434
No. of independent reflns	22022	25957	24070
No. of params	800	803	806
GOF on F^2	1.026	1.032	1.017
$R_1, wR_2 [I > 2\sigma(I)]$	0.0625, 0.1367	0.0591, 0.1245	0.0648, 0.1370
R_1, wR_2 [all data]	0.1056, 0.1602	0.1021, 0.1454	0.1148, 0.1618

and $\{[(\alpha\text{-PW}_{11}\text{O}_{39})\text{RE}(\text{H}_2\text{O})_2(\text{C}_2\text{O}_4)]^{10-} (\text{RE} = \text{Y}^{\text{III}}, \text{Dy}^{\text{III}}, \text{Ho}^{\text{III}} \text{ and } \text{Er}^{\text{III}})\}$ made by our group, to the best of our knowledge, **1Dy-3Yb** represent the third type of organic carboxylic acid bridging LSLKPs.

Upon adding organic amine cations or reducing the amount of K^+ ions, the POM precursor $[\text{P}_2\text{W}_{19}\text{O}_{69}(\text{H}_2\text{O})]^{14-}$ (Fig. 1a) easily decomposes into the monovacant Keggin-type $[\text{PW}_{11}\text{O}_{39}]^{7-}$ fragments in an acidic environment.¹⁷ Each monovacant Keggin-type $[\text{PW}_{11}\text{O}_{39}]^{7-}$ (Fig. 1b) fragment loses one WO_6 octahedra relative to the plenary Keggin $[\text{PW}_{12}\text{O}_{40}]^{3-}$ framework and has a defect site with four active oxygen atoms that can coordinate with Ln cations. After tartaric and $\text{DyCl}_3 \cdot 6\text{H}_2\text{O}$ are added in the solution, each Dy^{3+} ion is incorporated into the defect site of the $[\text{PW}_{11}\text{O}_{39}]^{7-}$ fragment and connects with oxygen atoms from the hydroxyl and carboxyl groups of tartaric ligands. Obviously, two tartaric ligands play a key bridging role in the construction of the dumbbell-like anion structure (Fig. 1c and Fig. S2 in the ESI†). There is much information on the configurations of the two tartaric ligands: the tartaric ligand containing C1, C2, C3 and C4 is the L-tartaric ligand, the other one containing C5, C6, C7 and C8 is the D-tartaric ligand, and both provide two terminal oxygen atoms and two oxygen atoms on α -carbon coordinating with the Dy^{3+} ions and form a kind of mesomeric complex (Fig. 1d and e). Notably, two nonequivalent Dy^{3+} ions are joined together by two tartaric acid groups with a distance of two Dy^{3+} ions ($\text{Dy1} \cdots \text{Dy2}$) of 6.049(2) Å. Moreover, both Dy^{3+} ions adopt eight-coordinate highly distorted square antiprism geometries (Fig. 1f and g), each of which is chelated by four O atoms from the monovacant polyanion $[\alpha\text{-PW}_{11}\text{O}_{39}]^{7-}$ and four O atoms from the two tartaric ligands. The eight-coordinate Dy1 atom is achieved by O23, O29, O36, O46 atoms from the defect site of the $[\text{PW}_{11}\text{O}_{39}]^{7-}$ subunit and O81, O83, O85, O89 atoms from one end of the two tartaric ligands with Dy1–O distances of 2.32(3)–2.52(3) Å. The two bottom planes of the square antiprism for the Dy1 centre are respectively defined by the oxygen atoms O23, O29, O36, and O46 and O81, O83, O85, and O89, and their average deviations from their least-squares planes are 0.0139 and 0.0878 Å, respectively. The dihedral angle for two bottom planes is 2.4°. The distances between the Dy1 atom and two bottom planes are 1.1278 and 1.4714 Å, respectively, and the O–Dy–O bond angles are in the range of 64.6(12)–148.3(11)°. The square antiprismatic geometry of the Dy2 centre is coordinated by O15, O40, O42, O43 atoms from another $[\text{PW}_{11}\text{O}_{39}]^{7-}$ subunit and O74, O86, O87 and O88 atoms from the other end of the two tartaric ligands with Dy2–O distances of 2.29(3)–2.46(3) Å, in which O15, O40, O42, and O43 atoms and O74, O86, O87, and O88 atoms constitute two bottom planes of the square antiprism and their average deviations from their least-squares planes are 0.0334 and 0.1044 Å, respectively. The dihedral angle for the two bottom surfaces is also 2.4°, the distances between the Dy2 atom and the two bottom planes are 1.1097 and 1.4519 Å, respectively and the corresponding O–Dy–O bond angles are in the range of 63.1(13)–146.9(12). The above-mentioned data indicate that the square antiprism is severely distorted, which may be related to the coordination environments from different coordination atoms.

Such a structure of **1Dy** is similar to those of the other two types of LSLKPs $\{[(\alpha\text{-PW}_{11}\text{O}_{39})\text{Ln}(\text{H}_2\text{O})(\eta^2, \mu-1, 1)\text{CH}_3\text{COO}]_2\}^{10-}$

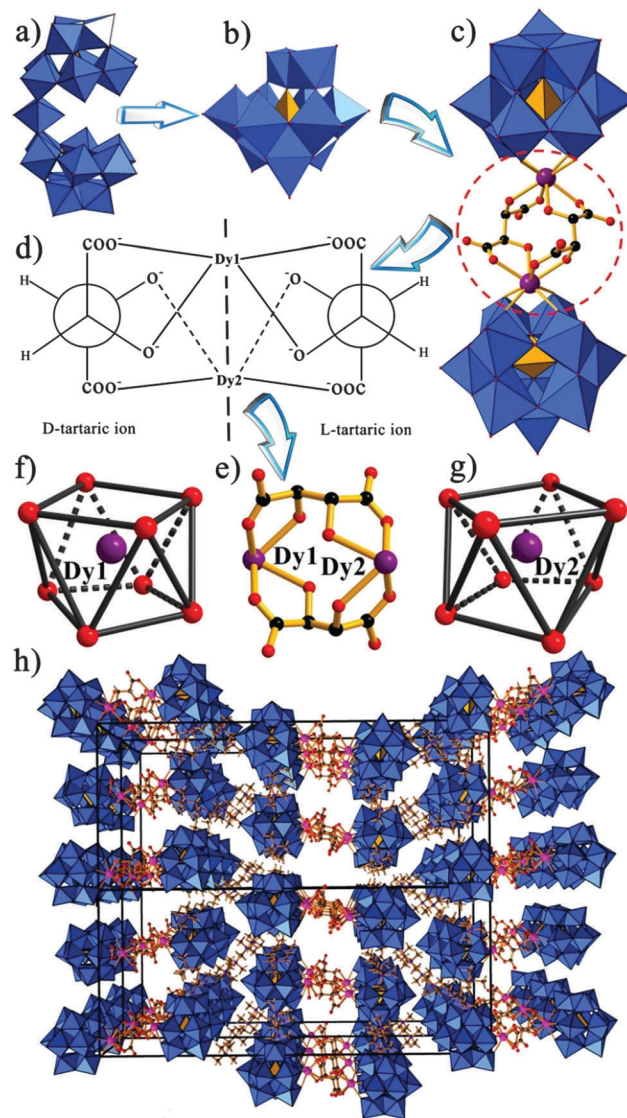


Fig. 1 Polyhedral representation of (a) the precursor $[\text{P}_2\text{W}_{19}\text{O}_{69}(\text{H}_2\text{O})]^{14-}$. (b) Polyhedral representation of the monovacant Keggin-type subunit $[\text{PW}_{11}\text{O}_{39}]^{7-}$. (c) The ball-and-stick/polyhedral representation of the dimeric polyoxoanions of **1Dy**. (d) The coordination environment of the D-tart and L-tart ligands in **1Dy**. (e) The coordination environment of the Dy1 and Dy2 atoms. (f) The square antiprismatic geometry of the Dy1 atom. (g) The square antiprismatic geometry of the Dy2 atom. (h) The packing arrangement of **1Dy** along the b axis. (Colour code: WO_6 = blue octahedra; PO_4 = orange tetrahedra; Dy = purple spheres; O = red spheres; C = black spheres, all the hydrogen atoms are omitted for clarity).

and $\{[(\alpha\text{-PW}_{11}\text{O}_{39})\text{RE}(\text{H}_2\text{O})_2(\text{C}_2\text{O}_4)]^{10-} (\text{RE} = \text{Y}^{\text{III}}, \text{Dy}^{\text{III}}, \text{Ho}^{\text{III}} \text{ and } \text{Er}^{\text{III}})\}$, which contain two eight-coordinate Ln^{III} cations with distorted square antiprism geometries and display a dimeric structure constructed by two mono-Ln substituted Keggin units. Nevertheless, there are also two obvious differences between them: (1) tartaric acid is a tetradentate ligand in contrast to acetic acid, which can link the two Dy-substituted $[\text{PW}_{11}\text{O}_{39}]^{7-}$; (2) tartaric acid has a longer carbon chain than acetic acid and oxalic acid, which can elongate the size of dimeric polyoxoanions from 21.9 to 24.9 Å (Fig. S3 in the ESI†). In addition, dimeric polyoxoanions $[(\alpha\text{-PW}_{11}\text{O}_{39})\text{Dy}(\text{C}_4\text{H}_2\text{O}_6)]_2^{16-}$

are arranged in parallel and stacked along the *b*-axis, forming a 3-D network with 1-D channels, in which the discrete $[(\text{CH}_3)_4\text{N}]^+$ cations and solvent water molecules are filled with abundant hydrogen bonding interactions (Fig. 1h and Fig. S4 in the ESI[†]).

Photochromism

Photochromic POM-based materials are types of important composite or hybrid materials, which are attractive and promising for applications in many fields.²⁰ Their photochromism not only depends on the chemical nature of each component, but also on the synergistic interactions between them. In the process, the charge transfer plays a key role in these photochromic materials, which usually display two broad absorption bands in the visible region after UV irradiation. One intensity-enhanced absorption band appearing at about 450–550 nm was attributed to d–d transitions; another broad band in the range of 600–800 nm was assigned to the electron-transfer process of the metal-to-metal extra intervalence charge-transfer (IVCT) ($\text{M}^{5+} \rightarrow \text{M}^{6+}$) ($\text{M} = \text{W}, \text{Mo}$).²¹ These IVCT processes implied that electron transfer occurred between POMs and organic substrates, converting POM anions to heteropolyblues with simultaneous oxidation of organic substrates. As a consequence, the POM units entrapped in the composite matrix could be reduced under UV irradiation, indicating a good photochromic appearance.

The powder samples of **1Dy–3Yb** display efficient photochromic behaviors in response to UV irradiation. As shown in Fig. 2a–c, the powder samples of **1Dy–3Yb** show white (for **1Dy** and **3Yb**) or pink (for **2Er**) color in the ground state, which

change to blue color within one hour (saturated state) upon UV irradiation (300 W Xe lamp). After the lamp was turned off, they gradually recovered their natural colors for about five days under ambient conditions (Fig. 2a–c). During the irradiation process, these compounds still maintained their backbone structures, which was confirmed by the agreement with PXRD patterns (Fig. S5 in the ESI[†]) and IR spectra (Fig. S6 in the ESI[†]) before and after irradiation. These phenomena indicate that these compounds display efficiently reversible photochromic behaviors (Fig. S7, ESI[†]).

The diffuse reflectance spectra of **1Dy–3Yb** were collected under ambient conditions in the range 300–800 nm and the reflectivity values derived from the Kubelka–Munk function were calculated. As represented in Fig. 2d–i, the optical gaps of these compounds in the ground state are higher than 3.50 eV (3.50 eV for **1Dy**, 3.53 eV for **2Er** and 3.52 eV for **3Yb**), which are similar to those of many reported organic–inorganic hybrid POM materials (usually 3.30–3.70 eV).^{7,20a,22} After illumination for one hour, their optical gaps obviously decrease to 3.39 eV for **1Dy**, 3.44 eV for **2Er** and 3.46 eV for **3Yb**, indicating that the photochromic reactions have been triggered after irradiation. In addition, the photosensitive properties of **1Dy–3Yb** have been further investigated by the time dependent solid-state diffuse reflectance and absorption spectroscopy (Fig. 2j–l and Fig. S8 in the ESI[†]). The absorption bands of **1Dy–3Yb** cover almost the whole visible region and their absorption intensities increase with the prolonged irradiation time. Some sharp absorption signals (especially for **2Er**) in the range of 350–800 nm

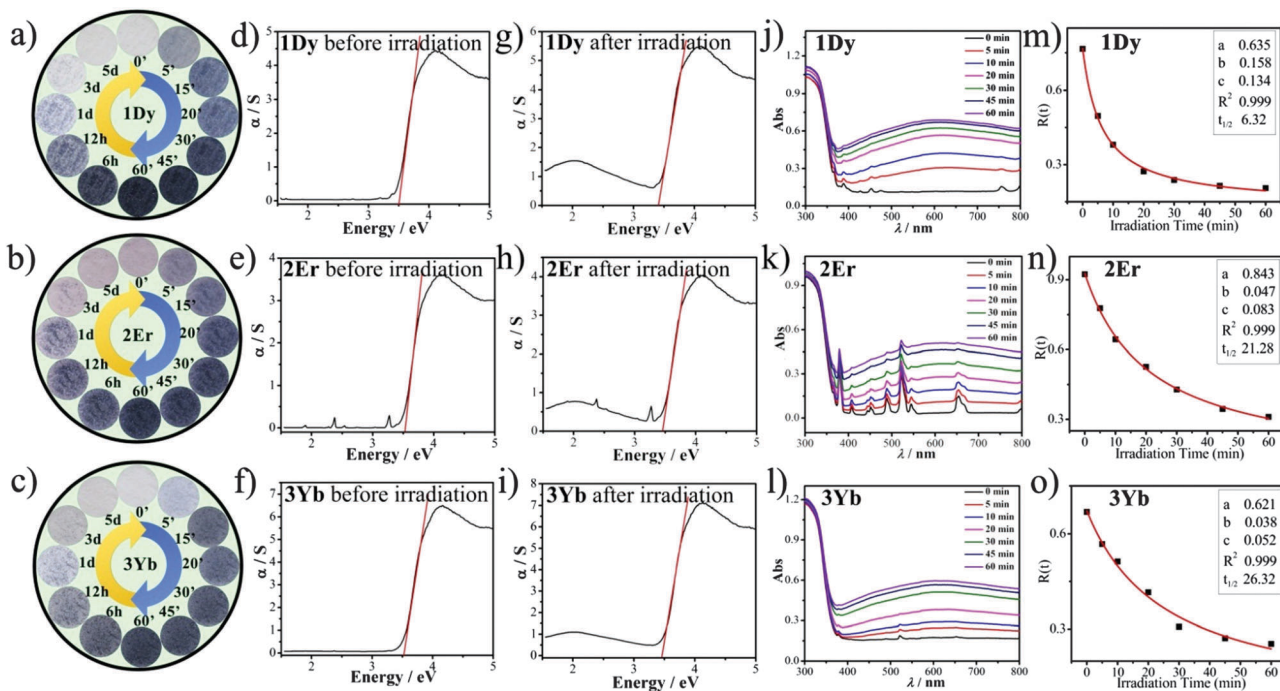


Fig. 2 (a–c) The color evolution for **1Dy**, **2Er**, and **3Yb** irradiated by a xenon lamp after 0, 5, 10, 15, 20, 30, 45, and 60 min and the color fading in the dark under ambient conditions after 6 h, 12 h, 1 d, 3 d and 5 d. (d–f) UV-vis diffuse reflectance spectra of K–M functions vs. energy (eV) for **1Dy**, **2Er**, and **3Yb** before irradiation. (g–i) UV-vis diffuse reflectance spectra of K–M functions vs. energy (eV) for **1Dy**, **2Er**, and **3Yb** after irradiation. (j–l) The evolutions of the solid-state diffuse reflectance absorption spectra of **1Dy**, **2Er**, and **3Yb** with irradiation times of 0, 5, 10, 20, 30, 45, and 60 min. (m–o) The plots of reflectivity $R(t)$ vs. t for **1Dy**, **2Er**, and **3Yb** measured at 605 nm for 0, 5, 10, 20, 30, 45, and 60 min irradiation by a xenon lamp.

are attributed to the f-f transitions of Ln cations. With increasing irradiation times, an obvious broad band at around 605 nm is observed in their absorption spectra, hinting the generation of mixed-valent W(v)/W(vi) species and the occurrence of $W^{5+} \rightarrow W^{6+}$ IVCT. The EPR spectra of the color-changed samples of **1Dy-3Yb** show noticeable paramagnetic signals with $g = 2.007, 2.006$ and 2.004 , respectively (Fig. S9 in the ESI[†]), indicating the existence of W^{5+} signals in the color-changed samples. The photochromic mechanism of **1Dy-3Yb** may be similar to the mechanism proposed by Hill's group and Wang's group,²³ in which the photoredox process maybe occur between solvation water molecules and POM anions by the proton transfer pathway of $O-H \cdots O_{POM}$ hydrogen bonds under high-power irradiation.

As we know, the appearance of a photogenerated color in hybrid materials usually takes place only on the surface of the irradiated samples. Therefore, the kinetics of coloration in **1Dy-3Yb** can be quantified by analyzing their reflectivity values $R(t)$ in the range of 300–800 nm as a function of the irradiation time (t) based on the diffuse reflectance spectra. According to the theory developed by Dessapt's group,²⁴ the reflectivity values at the maximum wavelength of the absorption ($R^{\lambda_{max}}$) versus the irradiation time (t) can be fitted by the function $R^{\lambda_{max}}(t) = a/(bt + 1) + R^{\lambda_{max}}(\infty) = a/(bt + 1) + c$, where the relative parameters a and b are proportionality constants and $c = R^{\lambda_{max}}(\infty)$. Alternatively, the speed of photoinduced coloration is also expressed by the half-life $t_{1/2}$ (the time required for $R(t)$ to reach the $[R(0) + R(\infty)]/2$) with the approximate half-life $t_{1/2} = 1/b$. As shown in Fig. 2m–o, the $R^{\lambda_{max}}$ values of **1Dy-3Yb** sharply decrease at first and then tend to be constant with the duration of irradiation, which is due to the decrease of concentration of the photoreduced W^{6+} . The coloration speeds signified by the coloration kinetic half-life times $t_{1/2}$ of **1Dy-3Yb** are listed in the inset in Fig. 2m–o, and these curves are fitted, giving $t_{1/2}$ values of 6.32 min for **1Dy**, 21.28 min for **2Er** and 26.32 min for **3Yb**. The results show that the coloration speed is in the order **1Dy** > **2Er** > **3Yb**, which is in accordance with the optical band gap order **1Dy** > **2Er** > **3Yb** during the photochromism.

Photoluminescence

Visible luminescence. Recently, Ln-based luminescent materials have been extensively investigated and have attracted large interest for their various applications in many lighting devices such as plasma display panels (PDPs), field emission displays (FEDs), liquid crystal displays (LCDs), and light-emitting diodes (LEDs).²⁵ In general, Ln ions were introduced into the appropriate hosts as activators to obtain the required phosphors based on their 4f-4f transitions, which can emit abundant colors upon excitation at particular wavelengths.²⁶ Therefore, the Ln ions can transfer specific photoluminescence properties to Ln-based POMs.

The emission spectrum of **1Dy** was recorded upon excitation with 367 nm UV light (Fig. S10 in the ESI[†]), it shows a characteristic emission of Dy^{3+} ions at 479, 573, and 662 nm (Fig. 3a) due to the intra-4f¹⁰ $^4F_{9/2} \rightarrow ^6H_J$ ($J = 15/2, 13/2, \text{ and } 11/2$) transitions, respectively.²⁷ The emission peaks at 479 and 662 nm correspond to the $^4F_{9/2} \rightarrow ^6H_{15/2}$ and $^4F_{9/2} \rightarrow ^6H_{11/2}$ transitions, respectively, whereas the intense emission peak at 573 nm is

attributed to a hypersensitive $^4F_{9/2} \rightarrow ^6H_{13/2}$ transition which is strongly influenced by the local environment of the Dy^{3+} ions.²⁸ It is noteworthy that the emission of **1Dy** is not a single sharp transition with the presence of well-splitting emission peaks, which may be ascribed to the crystal-field splitting effect.²⁹ The luminescence decay curve was recorded by monitoring the emission at 573 nm for the lifetime estimation and is shown in Fig. 3b. The obtained curve was well fitted with a biexponential decay to provide lifetimes of $\tau_1 = 21.64 \mu s$ (8.7%) and $\tau_2 = 77.28 \mu s$ (91.3%), which provides evidence of two Dy^{3+} emitting centres in **1Dy**. These lifetimes are evidently longer than most reported values in the literature.²⁸ For **2Er**, four groups of emission bands appear in the photoluminescence spectrum in Fig. 3c, the green emission at 558 nm with high-intensity is attributed to the $^4S_{3/2} \rightarrow ^4I_{15/2}$ transition with corresponding lifetimes of $\tau_1 = 1.02 \mu s$ (45.2%) and $\tau_2 = 9.35 \mu s$ (54.8%) (Fig. 3d); the two low-intensity green emission peaks at 546 and 532 nm are due to de-excitation of the $^4S_{3/2}$ and thermalized $^2H_{11/2}$ levels, respectively, whereas the transition from $^2H_{9/2}$ to $^4I_{11/2}$ levels gives rise to the weak peak observed in the red emission band at 700 nm, maybe resulting from the efficient cross-relaxation of $^4I_{11/2} + ^2G_{7/2} \rightarrow ^4F_{7/2} + ^2H_{11/2}/^4S_{3/2}$ between Er^{3+} ions.³⁰ In addition, the overall emission colors of the two samples are evaluated in terms of the standard CIE chromaticity diagram, which can be easily seen to be the yellowish green for **1Dy** and **2Er** (Fig. 3e).

Most strikingly, the fluorescence of **1Dy** displays an effectively switchable behavior when exposed to the UV light (Fig. 3f). Under the irradiation of a 300 W xenon lamp, the emission intensity (573 nm) decreases as the irradiation time increases and reaches 2.4% of the original value after 30 minutes accompanied by sample color deepening as well as absorption band strengthening. This phenomenon implies the intermolecular energy transfer from the excitation state of the Dy^{3+} ions to the colored state of POMs or radicals, which leads to a strong fluorescence quenching, perhaps because the emission bands of the luminescent components are partly overlapped with the absorption bands of the colored photoproduct (Fig. 2j–l and Fig. S8 in the ESI[†]). In addition, the emission intensity returns to its original value after the bleaching of **1Dy**. Therefore, the reversible photochromism of **1Dy** is responsible for its switchable luminescence. This result is similar to another photochromic and luminescent switchable hybrid POM reported recently.⁸ Compared to **1Dy**, **2Er** is less sensitive to UV light, which shows a little decline of the emission intensity with the increasing irradiation time (Fig. 3g).

Near-IR luminescence. The room-temperature NIR luminescence spectra of **1Dy-3Yb** are shown in Fig. 4. Upon excitation with visible light of 662 nm (Fig. S11a in the ESI[†]), **1Dy** shows the characteristic NIR luminescence of Dy^{3+} ions. The emission spectrum (Fig. 4a) consists of several bands at 864, 888, 997 and 1123 nm, which are attributed to the $^4F_{9/2} \rightarrow ^6H_{7/2} + ^6F_{9/2}, ^6H_{7/2}, ^6F_{5/2}, \text{ and } ^6F_{3/2}$ transitions, respectively.^{29,31} As for **2Er** (Fig. 4c), the characteristic emission for the Er^{3+} ions at 1533 nm is observed upon UV excitation (Fig. S11b in the ESI[†]), which corresponds to the $^4I_{13/2} \rightarrow ^4I_{15/2}$ transition.^{25d,30b,32} For **3Yb**, the NIR emission spectrum exhibits the $Yb^{3+} \ ^2F_{5/2} \rightarrow ^2F_{7/2}$

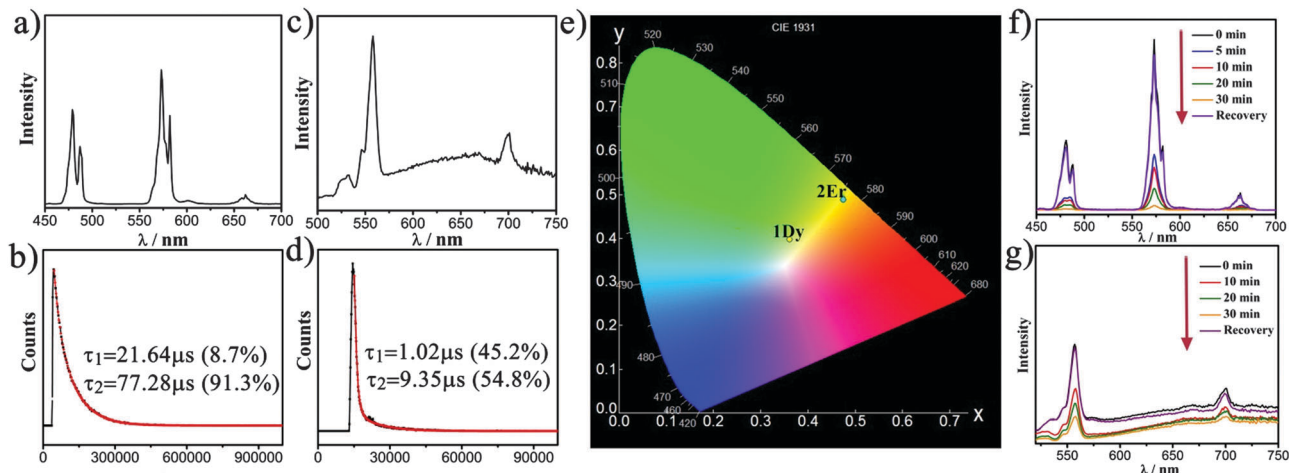


Fig. 3 (a) Emission spectrum (upon 367 nm excitation) of **1Dy**. (b) The decay curve of **1Dy**. (c) The emission spectrum (upon 380 nm excitation) of **2Er**. (d) The decay curve of **2Er**. (e) CIE chromaticity diagrams of **1Dy** and **2Er**. (f) The emission spectral evolution of **1Dy** (upon 367 nm excitation) after UV-irradiation (300 W Xe lamp) for different times and its recovery on exposure to air for 5 days. (g) The emission spectral evolution of **2Er** (upon 380 nm excitation) after UV-irradiation (300 W Xe lamp) for different times and its recovery spectrum on exposure to air for 5 days.

transition (Fig. 4e), the NIR characteristic emission for the Yb^{3+} ion at 980 nm is observed upon UV excitation (Fig. S11c in the ESI[†]).^{30b} The solid-state fluorescence lifetimes of **1Dy–3Yb** are also studied at room temperature (Fig. 4b, d and f), their decay behaviors are also fitted to a biexponential function as $I = A_1 \exp(-t/\tau_1) + A_2 \exp(-t/\tau_2)$, affording lifetimes of 1.96 μs (7.2%) and 11.30 μs (92.8%) for **1Dy**, 0.94 μs (42.5%) and 9.34 μs (57.5%) for **2Er**, and 1.87 μs (49.0%) and 8.95 μs (51.0%) for **3Yb**.

Magnetic properties

Static magnetic properties of 1Dy–3Yb. The temperature dependencies of the molar susceptibility data for **1Dy–3Yb** were studied under an applied direct current (dc) field of 1000 Oe from 300 to 2 K (Fig. 5a). The room-temperature $\chi_{\text{M}}T$ value of 28.18 $\text{cm}^3 \text{K mol}^{-1}$ for **1Dy** is in good agreement with that expected for two non-interacting Dy^{III} ions of 28.34 ($^6\text{H}_{15/2}$, $S = 5/2$, $L = 5$, $g = 4/3$) and decreases to 16.14 $\text{cm}^3 \text{K mol}^{-1}$ at 2 K. For **2Er**, the $\chi_{\text{M}}T$ value of 23.86 $\text{cm}^3 \text{K mol}^{-1}$ at 300 K is slightly higher than the spin-only value of two uncoupled Er^{III} ions of 22.96 $\text{cm}^3 \text{K mol}^{-1}$ ($^4\text{I}_{15/2}$, $S = 3/2$, $L = 6$, $g = 6/5$). As the temperature is lowered, the $\chi_{\text{M}}T$ value undergoes a gradual reduction and then a sharp decrease below 60 K and reaches a minimum of 13.55 $\text{cm}^3 \text{K mol}^{-1}$ at 2 K. As for **3Yb**, the $\chi_{\text{M}}T$ value of 4.46 $\text{cm}^3 \text{K mol}^{-1}$ at 300 K is slightly smaller than the theoretic value of 5.14 $\text{cm}^3 \text{K mol}^{-1}$ of two isolated Yb^{3+} ions ($^2\text{F}_{7/2}$, $S = 1/2$, $L = 3$, $g = 8/7$). Upon cooling, the $\chi_{\text{M}}T$ product gradually decreases to a minimum of 2.53 $\text{cm}^3 \text{K mol}^{-1}$ at 2 K. The behaviors of decreasing $\chi_{\text{M}}T$ values for **1Dy–3Yb** upon cooling are attributed to the depopulation of the excited Stark sublevels originating from spin–orbit coupling and ligand-field effects.³³ In addition, the susceptibility data of **1Dy–3Yb** obey the Curie–Weiss law (Fig. S12 in the ESI[†]), with $C = 29.67 \text{ cm}^3 \text{K mol}^{-1}$ and $\theta = -21.41 \text{ K}$ for **1Dy** above 50 K and $C = 24.30 \text{ cm}^3 \text{K mol}^{-1}$ and $\theta = -5.88 \text{ K}$ for **2Er** between 2 and 300 K and $C = 4.92 \text{ cm}^3 \text{K mol}^{-1}$ and $\theta = -30.42 \text{ K}$ for **3Yb** above 50 K.

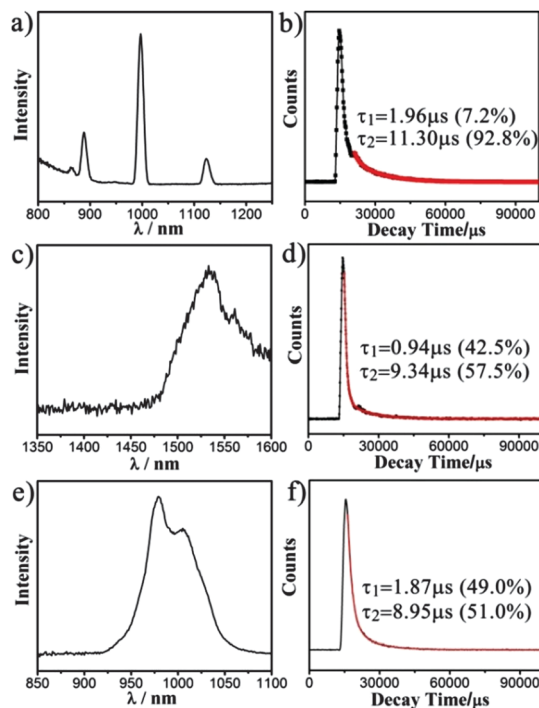


Fig. 4 NIR emission spectra and decay curves (a) and (b) of **1Dy**, (c) and (d) of **2Er**, (e) and (f) of **3Yb**.

The field dependent magnetizations for **1Dy–3Yb** measured in the 2–8 K temperature range show the fast rise in low fields followed by a gradual increase to the maximum values at 7 T (Fig. 5b–d). The magnetizations for the three compounds at 2 K increase very rapidly at lower magnetic field (below 1 T for **1Dy** and **2Er**, below 2 T for **3Yb**) and then a slow increase is observed without saturation up to 7 T, whereas the magnetization increases slowly as the magnetic field increases upon increasing the temperature. The magnetization values at 2 K (10.0 N β , 10.9 N β , and 3.4 N β for **1Dy–3Yb**, respectively)

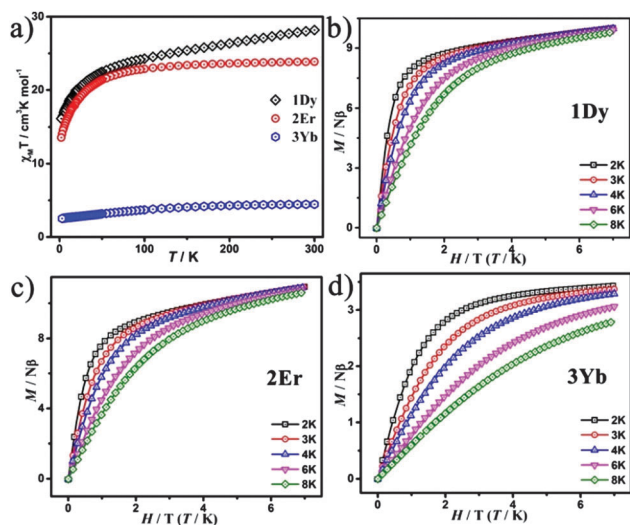


Fig. 5 (a) Plots of $\chi_M T$ vs. T at 1000 Oe for the powder samples of **1Dy**, **2Er**, and **3Yb**. Plots of magnetisation (M) versus magnetic field for **1Dy** (b), **2Er** (c), and **3Yb** (d) between 2 and 8 K.

at high magnetic fields are much lower than their theoretically values, indicating the presence of magnetic anisotropy and/or a low-lying excited state of the Ln ions in **1Dy–3Yb**.³⁴ Furthermore, the non-superposition of the M versus H/T curves implies the presence of significant magnetic anisotropy.

Dynamic magnetic properties of 1Dy. Alternate current (ac) magnetic susceptibility measurements were performed for **1Dy–3Yb** to probe dynamic magnetic behaviors, only **1Dy** displays the possible SMM behavior. In the absence of a dc field, the frequency dependence of out-of-phase (χ_M'') signals of ac susceptibility for **1Dy** can be observed below 15 K, revealing the presence of slow relaxation of the magnetization (Fig. 6a and b). However, no peak maxima are observed for χ_M'' above 2 K, which can be attributed to quantum tunneling of the magnetization (QTM) often observed in Ln-based SMMs that diminishes the relaxation barriers. Generally, a static magnetic field was applied to suppress any possible QTM of Ln-based SMMs. To determine the optimum dc field, the ac susceptibility

measurements at various static fields (0–4000 Oe) were performed at 2 K (Fig. 6 and 7). Upon increasing the magnetic field from 0 Oe to 3000 Oe, the in-phase (χ_M') signals increasingly reveal the frequency dependence, the peak maxima are observed for χ_M' at 3000 Oe and the looming peaks for χ_M'' appear at 3000 Oe, indicating that the QTM is gradually suppressed. When a 4 kOe dc field is applied, the χ_M'' susceptibility curves clearly show frequency dependent peaks below 15 K between 100 and 10 000 Hz (Fig. 7), indicative of the field-induced SMM behavior. Moreover, the ac susceptibility data collected at the applied static field of 4 kOe show that the peak around 4.5 K hardly shifts, which maybe resulting from large field-induced intermolecular interactions rather than arising from the molecular origin. Such a behavior is occasionally observed in previous studies of SMMs.³⁵ The relaxation time (τ) between 2 and 6.5 K was estimated by fitting the τ versus the reciprocal temperature based on the Arrhenius plot in Fig. 7c. Using the Arrhenius law [$\tau = \tau_0 \exp(U_{\text{eff}}/k_B T)$], the analysis of the data gives a calculated effective energy barrier of $U_{\text{eff}} = 20$ K and a τ_0 value of 4.2×10^{-7} s for the thermally activated regime above 4.0 K, which is consistent with the expected τ_0 value of 10^{-6} – 10^{-11} s for a SMM.^{35,36} The relatively small barrier is observed as a result of the QTM, which is common in the Ln-based SMMs.^{35,36} An incomplete semicircle Cole–Cole curve (the inset of Fig. 7c) in the form of the χ_M'' versus χ_M' curve was obtained, which was fitted by using a generalized Debye model. The large distribution coefficient value of α is 0.53, implying that the thermally activated relaxation processes accompany a large distribution of relaxation time. Similar behaviors have been usually observed in Dy-based compounds.³⁷

In addition, magnetization hysteresis is another important characteristic of a SMM in the magnetic system with slow magnetic relaxation. Therefore, the low temperature hysteresis loops were measured on microcrystalline samples using a SQUID-VSM magnetometer, in order to further explore the dynamic behavior of **1Dy**. As shown in Fig. 7d and Fig. S13 (in the ESI[†]), a narrow butterfly-shaped hysteresis loop at around zero dc field is clearly observed below 5 K within ± 10 kOe at a sweeping rate of 500 Oe s^{-1} . When the temperature drops down to 2 K, the

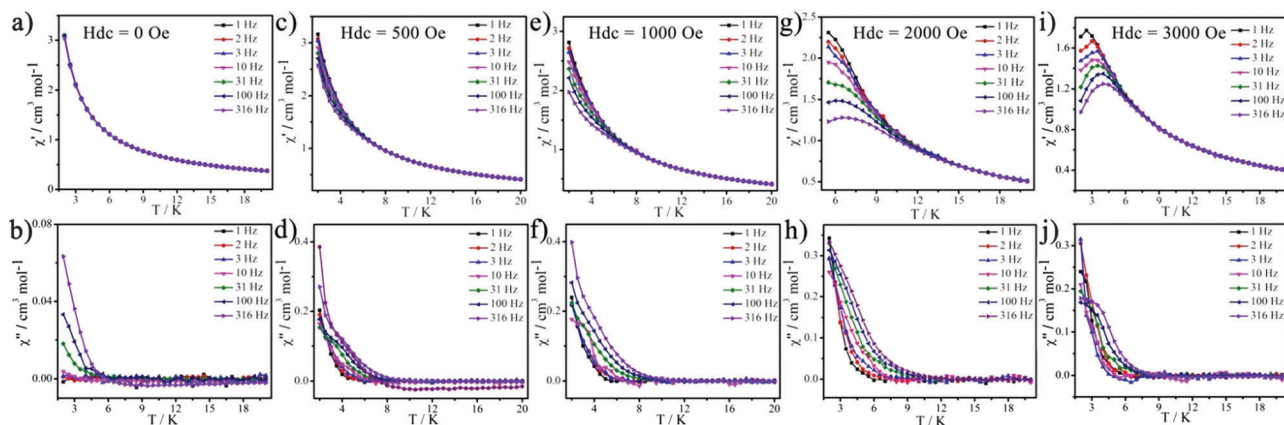


Fig. 6 Temperature dependence of the in-phase (χ_M') and out-of-phase (χ_M'') signals from the AC susceptibility measurements of **1Dy** with an applied static field of 0 Oe (a and b), 500 Oe (c and d), 1000 Oe (e and f), 2000 Oe (g and h), and 3000 Oe (i and j).

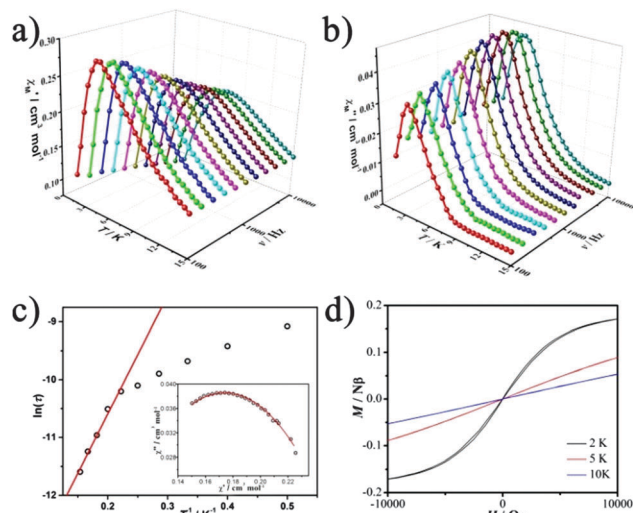


Fig. 7 Frequency dependence of the in-phase (χ''_M') (a) and out-of-phase (χ''_M'') (b) signals under 4 kOe dc fields for **1Dy** at 2 K. (c) The magnetization relaxation time $\ln(\tau)$ versus $1/T$ plot for **1Dy** represented with the solid red line corresponds to the Arrhenius law. The inserted Cole–Cole plot under a 4 kOe external field at 4.5 K for **1Dy** denoted with the solid red line represents the best fitting to the generalized Debye model. (d) Hysteresis loops for **1Dy** measured at different temperatures at a sweeping rate of 500 Oe s⁻¹.

butterfly-shaped hysteresis loop becomes obvious, which is consistent with the dominant QTM often observed for Ln systems.³⁸ As the field increases, the loop becomes broader with a maximum occurring between 3 and 5 kOe, being in agreement with the ac optimum field of 4 kOe. Upon decreasing the field sweep rate to 100 Oe s⁻¹, QTM becomes more obvious and the loop becomes narrower and almost invisible, indicating the dynamic behavior of **1Dy**.³⁸ This dynamic magnetic behavior of the dependence of hysteresis loops on the temperature and field sweep rate is exactly consistent with that observed in the ac susceptibility data.

Conclusions

In conclusion, we have reported herein a series of inorganic–organic hybrid crystalline materials containing double-tartaric bridging mono-Ln substituted POMs, which, to the best of our knowledge, represent the third type of organic carboxylic acid bridging LSLKPs. This structural type of organic hybrid LSLKPs is governed by the coordination behaviors of carboxylate linkers. Most importantly, these compounds stand for a kind of significant POM-based multifunctional crystalline materials involving POM units, Ln ions and organic components, which embody the coexistence of photochromic, luminescence and magnetic properties. To our knowledge, **1Dy** represents the first POM-based multifunctional material combining reversible photochromic, switchable luminescence and SMM properties. Therefore, the developed inorganic–organic hybrid POMs are promising for their multifunctional applications. This research provides a possible methodology for fabricating novel multifunctional

crystalline materials by selecting appropriate POM precursors, Ln cations and organic components. In future, we will further explore this field by adjusting different reaction components. We believe that this work may stimulate and promote the development of POM chemistry and materials chemistry.

Acknowledgements

We gratefully acknowledge support from the NSFC and the Foundation of Education Department of Henan Province (No. 14A150028).

Notes and references

- (a) R. Pardo, M. Zayat and D. Levy, *Chem. Soc. Rev.*, 2011, **40**, 672; (b) T. Zhang and W. Lin, *Chem. Soc. Rev.*, 2014, **43**, 5982; (c) J.-S. Li, X.-J. Sang, W.-L. Chen, L.-C. Zhang, Z.-M. Zhu, T.-Y. Ma, Z.-M. Su and E.-B. Wang, *ACS Appl. Mater. Interfaces*, 2015, **7**, 13714; (d) A. Dolbecq, E. Dumas, C. R. Mayer and P. Mialane, *Chem. Rev.*, 2010, **110**, 6009; (e) C.-C. Wang, J.-R. Li, X.-L. Lv, Y.-Q. Zhang and G. Guo, *Energy Environ. Sci.*, 2014, **7**, 2831; (f) A. Saad, O. Oms, J. Marrot, A. Dolbecq, K. Hakouk, H. El Bekkachi, S. Jobic, P. Deniard, R. Dessapt, D. Garrot, K. Boukheddaden, R. Liu, G. Zhang, B. Keita and P. Mialane, *J. Mater. Chem. C*, 2014, **2**, 4748; (g) J.-B. Peng, X.-J. Kong, Q.-C. Zhang, M. Orendáč, J. Prokleška, Y.-P. Ren, L.-S. Long, Z. Zheng and L.-S. Zheng, *J. Am. Chem. Soc.*, 2014, **136**, 17938.
- (a) C. Zou, Z. Zhang, X. Xu, Q. Gong, J. Li and C.-D. Wu, *J. Am. Chem. Soc.*, 2012, **134**, 87; (b) D. MasPOCH, D. Ruiz-Molina and J. Veciana, *Chem. Soc. Rev.*, 2007, **36**, 770.
- (a) H. Zhang, G. Chen and D. W. Bahnemann, *J. Mater. Chem.*, 2009, **19**, 5089; (b) N. Gao, H. Sun, K. Dong, J. Ren, T. Duan, C. Xu and X. Qu, *Nat. Commun.*, 2014, **5**, 3422; (c) D. Liu, Y. Lu, H.-Q. Tan, W.-L. Chen, Z.-M. Zhang, Y.-G. Li and E.-B. Wang, *Chem. Commun.*, 2013, **49**, 3673; (d) S. Omwoma, C. T. Gore, Y. Ji, C. Hu and Y.-F. Song, *Coord. Chem. Rev.*, 2015, **286**, 17; (e) H. N. Miras, J. Yan, D.-L. Long and L. Cronin, *Chem. Soc. Rev.*, 2012, **41**, 7403.
- (a) J.-Z. Liao, H.-L. Zhang, S.-S. Wang, J.-P. Yong, X.-Y. Wu, R. Yu and C.-Z. Lu, *Inorg. Chem.*, 2015, **54**, 4345; (b) J. J. Walsh, A. M. Bond, R. J. Forster and T. E. Keyes, *Coord. Chem. Rev.*, 2016, **306**(1), 217; (c) T. Yamase, *Chem. Rev.*, 1998, **98**, 307.
- P. Mialane, G. Zhang, I. M. Mbomekalle, P. Yu, J. D. Compain, A. Dolbecq, J. Marrot, F. Secheresse, B. Keita and L. Nadjo, *Chem. – Eur. J.*, 2010, **16**, 5572.
- Y. Wang, H. Li, C. Wu, Y. Yang, L. Shi and L. Wu, *Angew. Chem., Int. Ed.*, 2013, **52**, 4577.
- Y. Liang, S. Li, D. Yang, P. Ma, J. Niu and J. Wang, *J. Mater. Chem. C*, 2015, **3**, 4632.
- D.-F. Shen, S. Li, H. Liu, W. Jiang, Q. Zhang and G.-G. Gao, *J. Mater. Chem. C*, 2015, **3**, 12090.
- (a) D. T. de Lill, A. de Bettencourt-Dias and C. L. Cahill, *Inorg. Chem.*, 2007, **46**, 3960; (b) J. Xia, B. Zhao, H.-S. Wang,

- W. Shi, Y. Ma, H.-B. Song, P. Cheng, D.-Z. Liao and S.-P. Yan, *Inorg. Chem.*, 2007, **46**, 3450.
- 10 (a) R. D. Peacock and T. J. R. Weakley, *J. Chem. Soc. A*, 1971, 1836; (b) C. Zhang, R. C. Howell, K. B. Scotland, F. G. Perez, L. Todaro and L. C. Francesconi, *Inorg. Chem.*, 2004, **43**, 7691; (c) J. Iijima, E. Ishikawa, Y. Nakamura and H. Naruke, *Inorg. Chim. Acta*, 2010, **363**, 1500.
- 11 J. Niu, K. Wang, H. Chen, J. Zhao, P. Ma, J. Wang, M. Li, Y. Bai and D. Dang, *Cryst. Growth Des.*, 2009, **9**, 4362.
- 12 C. Zhang, P. Ma, H. Chen, J. Wang and J. Niu, *J. Coord. Chem.*, 2011, **64**, 2178.
- 13 P. Ma, Y. Si, R. Wan, S. Zhang, J. Wang and J. Niu, *Spectrochim. Acta, Part A*, 2015, **138**, 579.
- 14 (a) X. Fang, T. M. Anderson, W. A. Neiwert and C. L. Hill, *Inorg. Chem.*, 2003, **42**, 8600; (b) R. Khoshnavazi and S. Tayamon, *J. Coord. Chem.*, 2010, **63**, 3356; (c) R. Khoshnavazi, F. Nicolò, H. Amiri Rudbari, E. Naseri and A. Aminipour, *J. Coord. Chem.*, 2013, **66**, 1374.
- 15 F. L. Sousa, F. A. Almeida Paz, A. M. V. Cavaleiro, J. Klinowski and H. I. S. Nogueira, *Chem. Commun.*, 2004, 2656.
- 16 S. Zhang, Y. Wang, J. Zhao, P. Ma, J. Wang and J. Niu, *Dalton Trans.*, 2012, **41**, 3764.
- 17 C. M. Tourne and G. F. Tourne, *J. Chem. Soc., Dalton Trans.*, 1988, 2411.
- 18 G. M. Sheldrick, *SADABS–Bruker AXS area detector scaling and absorption version 2008/2001*, University of Göttingen, Germany, 2008.
- 19 G. M. Sheldrick, *Acta Crystallogr., Sect. A: Found. Crystallogr.*, 2008, **64**, 112.
- 20 (a) J.-D. Compain, P. Deniard, R. Dessapt, A. Dolbecq, O. Oms, F. Secheresse, J. Marrot and P. Mialane, *Chem. Commun.*, 2010, **46**, 7733; (b) R. Dessapt, M. Gabard, M. Bujoli-Doeuff, P. Deniard and S. Jobic, *Inorg. Chem.*, 2011, **50**, 8790; (c) K. Hakouk, O. Oms, A. Dolbecq, H. El Moll, J. Marrot, M. Evain, F. Molton, C. Duboc, P. Deniard, S. Jobic, P. Mialane and R. Dessapt, *Inorg. Chem.*, 2013, **52**, 555.
- 21 (a) E. Papaconstantinou, *Chem. Soc. Rev.*, 1989, **18**, 1; (b) T. He and J. Yao, *Prog. Mater. Sci.*, 2006, **51**, 810.
- 22 H. El Moll, A. Dolbecq, I. M. Mbomekalle, J. Marrot, P. Deniard, R. Dessapt and P. Mialane, *Inorg. Chem.*, 2012, **51**, 2291.
- 23 (a) M. M. Williamson, D. A. Bouchard and C. L. Hill, *Inorg. Chem.*, 1987, **26**, 1436; (b) H. Zhang, L. Duan, Y. Lan, E. Wang and C. Hu, *Inorg. Chem.*, 2003, **42**, 8053.
- 24 R. Dessapt, M. Collet, V. Coué, M. Bujoli-Doeuff, S. Jobic, C. Lee and M.-H. Whangbo, *Inorg. Chem.*, 2009, **48**, 574.
- 25 (a) S.-S. Wang, W.-T. Chen, Y. Li, J. Wang, H.-S. Sheu and R.-S. Liu, *J. Am. Chem. Soc.*, 2013, **135**, 12504; (b) Y. Liu, D. Tu, H. Zhu and X. Chen, *Chem. Soc. Rev.*, 2013, **42**, 6924; (c) X. Liu, C. Li, Z. Quan, Z. Cheng and J. Lin, *J. Phys. Chem. C*, 2007, **111**, 16601; (d) K. Binnemans, *Chem. Rev.*, 2009, **109**, 4283.
- 26 (a) D. Kim, J. Jang, S. I. Ahn, S.-H. Kim and J.-C. Park, *J. Mater. Chem. C*, 2014, **2**, 2799; (b) K.-W. Huang, W.-T. Chen, C.-I. Chu, S.-F. Hu, H.-S. Sheu, B.-M. Cheng, J.-M. Chen and R.-S. Liu, *Chem. Mater.*, 2012, **24**, 2220.
- 27 (a) P. Ma, R. Wan, Y. Si, F. Hu, Y. Wang, J. Niu and J. Wang, *Dalton Trans.*, 2015, **44**, 11514; (b) Y.-L. Wang, B. Gu, Y. Ma, C. Xing, Q.-L. Wang, L.-C. Li, P. Cheng and D.-Z. Liao, *CrystEngComm*, 2014, **16**, 2283.
- 28 (a) S. Biju, N. Gopakumar, J. C. G. Bünzli, R. Scopelliti, H. K. Kim and M. L. P. Reddy, *Inorg. Chem.*, 2013, **52**, 8750; (b) P. Bag, C. K. Rastogi, S. Biswas, S. Sivakumar, V. Mereacre and V. Chandrasekhar, *Dalton Trans.*, 2015, **44**, 4328.
- 29 J. Feng, H.-J. Zhang, S.-Y. Song, Z.-F. Li, L.-N. Sun, Y. Xing and X.-M. Guo, *J. Lumin.*, 2008, **128**, 1957.
- 30 (a) J. Cichos, L. Marciniak, D. Hreniak, W. Strek and M. Karbowski, *J. Mater. Chem. C*, 2014, **2**, 8244; (b) R. Krishnan and J. Thirumalai, *New J. Chem.*, 2014, **38**, 3480; (c) D. He, C. Guo, S. Zhou, L. Zhang, Z. Yang, C. Duan and M. Yin, *CrystEngComm*, 2015, **17**, 7745.
- 31 S. Su, W. Chen, C. Qin, S. Song, Z. Guo, G. Li, X. Song, M. Zhu, S. Wang, Z. Hao and H. Zhang, *Cryst. Growth Des.*, 2012, **12**, 1808.
- 32 C. M. Granadeiro, R. A. S. Ferreira, P. C. R. Soares-Santos, L. s. D. Carlos and H. I. S. Nogueira, *Eur. J. Inorg. Chem.*, 2009, 5088.
- 33 (a) Z.-R. Jhu, C.-I. Yang and G.-H. Lee, *CrystEngComm*, 2013, **15**, 2456; (b) H. Xiang, Y. Lan, H.-Y. Li, L. Jiang, T.-B. Lu, C. E. Anson and A. K. Powell, *Dalton Trans.*, 2010, **39**, 4737.
- 34 B.-L. H. W.-B. Sun, P.-H. Lin, H.-F. Li, P. Chen, Y.-M. Tian, M. Murugesu and P.-F. Yan, *Dalton Trans.*, 2013, **42**, 13397.
- 35 (a) N. J. Yutronkie, I. A. Kuhne, I. Korobkov, J. L. Brusso and M. Murugesu, *Chem. Commun.*, 2016, **52**, 677; (b) F. Habib, I. Korobkov and M. Murugesu, *Dalton Trans.*, 2015, **44**, 6368.
- 36 A. J. Calahorra, I. Oyarzabal, B. Fernandez, J. M. Seco, T. Tian, D. Fairen-Jimenez, E. Colacio and A. Rodriguez-Dieguez, *Dalton Trans.*, 2016, **45**, 591.
- 37 H.-L. Gao, L. Jiang, S. Liu, H.-Y. Shen, W.-M. Wang and J.-Z. Cui, *Dalton Trans.*, 2016, **45**, 253.
- 38 (a) D.-D. Yin, Q. Chen, Y.-S. Meng, H.-L. Sun, Y.-Q. Zhang and S. Gao, *Chem. Sci.*, 2015, **6**, 3095; (b) Q. Chen, Y.-S. Meng, Y.-Q. Zhang, S.-D. Jiang, H.-L. Sun and S. Gao, *Chem. Commun.*, 2014, **50**, 10434; (c) Y.-N. Guo, G.-F. Xu, W. Wernsdorfer, L. Ungur, Y. Guo, J. Tang, H.-J. Zhang, L. F. Chibotaru and A. K. Powell, *J. Am. Chem. Soc.*, 2011, **133**, 11948.